Nano Energy 27 (2016) 87–94

Contents lists available at ScienceDirect

Nano Energy

journal homepage: www.elsevier.com/locate/nanoen

Controlled orientation of perovskite films through mixed cations toward high performance perovskite solar cells

Guangda Niu, Hongde Yu, Jiangwei Li, Dong Wang, Liduo Wang *

Department of Chemistry, Tsinghua University, 100084, Beijing, China

ARTICLE INFO

Article history:
Received 18 March 2016
Received in revised form
27 June 2016
Accepted 27 June 2016
Available online 28 June 2016

Keywords:
Perovskite solar cells
Orientation
Doping

ABSTRACT

Solar cells based on organic inorganic hybrid metal halide perovskites have exhibited a rapid increase of power conversion efficiency (PCE). Perovskite solar cells involving mixed cations, especially recently reported Cs doping, have shown huge potential to improve PCE as well as device stability. However, when doping Cs into $CH_3NH_3PbI_3$ ($MAPbI_3$) and $[HC(NH_2)_2]_3PbI_3$ ($FAPbI_3$), $CsPbI_3$ could segregate from the perovskite phase, affecting the performance negatively. In addition, despite improved charge transfer was predicted for oriented film along $<112>/<200>$ directions, the fabrication is still on the way and rarely reported. Herein, an ultra-smooth perovskite film oriented along $<112>/<200>$ directions is created for the first time, with a homogeneous tetragonal phase of $(MAPbI_3)_{1-x}(CsPbBr_3)_x$. The preferentially precipitated heavily Cs-doped perovskite, and the lowered surface energy of (112) and (200) planes, verified by DFT calculations, are responsible for the orientation. The improved charge transfer and suppressed trap states in the oriented film substantially improved the performance. Upon an optimal doping ratio of 0.1, a PCE of 17.6% was achieved, together with remarkable improvements in stability under UV irradiance and in ambient atmosphere.

© 2016 Elsevier Ltd. All rights reserved.

1. Introduction

Solar cells based on organic inorganic hybrid metal halide perovskites have received increasing attention due to their rapid increase of power conversion efficiency (PCE), from 9.7% to 22.1% in only two years [1–3]. The perovskites, as light-absorber component, exhibit broad absorption spectra, large extinction coefficient, high carrier mobility, as well as ambipolar charge transport [4–6]. Despite the amazing performance, there is still a huge gap between academic studies and industrial applications on account of the poor stability [7]. $CH_3NH_3PbI_3$ ($MAPbI_3$), the most commonly used perovskite, is vulnerable to the humidity, heat, and UV light conditions [8–10]. For this reason, doping has been demonstrated as an effective method to improve the stability and photovoltaic performance. For example, due to a more compact and stable crystal structure compared to $MAPbI_3$, mixed halide perovskite $MAPb(I_{1-x}Br_x)_3$ is resistant to the moisture [11]. Cs-doped $[HC(NH_2)_2]_3PbI_3$ ($FAPbI_3$) film exhibits merits on both the moisture and light soaking stability [12]. However, when introducing Cs into $MAPbI_3$, the yellow orthorhombic phase of $CsPbI_3$ easily segregated from the film, especially for higher doping content, restricting the performance [13].

In addition, when involving exotic species into the precursor solutions, the crystallization during film formation process, is expected to change, which determines the morphology of the film, and the cell performance. Recently, McGehee and co-workers observed a Cl-rich precursor phase presented in the early stage during $MAPbI_{3-x}Cl_x$ formation, which is responsible for the final oriented perovskite film along $<110>$ direction[14]. Meanwhile, it is strikingly found that for Cs-doped $FAPbI_3$ and CsPbI3 film, the orientation changed as Cs involved into the film [15,16]. Whereas, the underlying mechanism for the different orientation compared to pure $MAPbI_3$ and $FAPbI_3$ is still not clear. According to the experimental and theoretical results, the orientation indeed has a critical influence on the film, such as the stress, the morphology, and even the charge transfer between perovskite and substrate [17–19]. So far, $MAPbI_3$ and $MAPbI_{3-x}Cl_x$ film generally exhibit preferred orientation along $<110>$ and/or $<002>$ directions. Although the orientation along $<112>$ and $<200>$ directions is calculated to be beneficial for the carrier transfer, the fabrication has been reported by only a few papers [19–21]. The success is limited in terms of the rough surface or only partially orientation along $<112>$ and $<200>$ directions, making the comparison of photovoltaic performance unconvincing. It is still highly challenging to obtain flat perovskite film with well-controlled orientation along $<112>$ and $<200>$ directions. To better understand the formation process of oriented film, fabrication of perovskite film with controlled orientation directions is of vital urgency and significance.

* Corresponding author.
E-mail address: chldwang@mail.tsinghua.edu.cn (L. Wang).

http://dx.doi.org/10.1016/j.nanoen.2016.06.053
2211-2855/© 2016 Elsevier Ltd. All rights reserved.

In this paper, we successfully fabricated ultra-smooth perovskite films oriented along <112>/<200> directions for the first time, with a homogeneous perovskite phase of $(MAPbI_3)_{1-x}(CsPbBr_3)_x$. In contrast, before doping, $MAPbI_3$ exhibited orientation along <110>/<002> directions. We systematically studied the formation mechanism of the oriented film along <112>/<200> directions. It was found that the selective precipitate of CsX together with PbX_2 in the early stage (where X represents halogen) served as the heterogeneous nucleation sites and formed heavily Cs-doped perovskite in the bottom of the film. Combined with the specific surface energy calculations, the heavily Cs-doped perovskite lowered the surface energy of (112)/(200) planes and initiated the growth along corresponding directions under thermodynamic control. As to the photovoltaic performance, when the doping content increased, the short circuit currents (J_{sc}) gradually decreased, while the open circuit voltages (V_{oc}) and fill factors (FF) enhanced, resulting in a power conversion efficiency as high as 17.6% upon an optimal doping ratio of 0.1. The enhancement of FF attributed to the improved charge transfer in the oriented film along <112>/<200> directions and thus reduced series resistance. In addition, the suppressed trap states of perovskite, due to the altered orientation as well as Cs involvement, helped restrain the internal charge recombination process and contributed to the higher V_{oc} values. Importantly, compared to pure $MAPbI_3$, doping of $CsPbBr_3$ into the film greatly improved the device stability toward UV light as well as moisture.

2. Results and discussion

Here we employed a one-step method to deposit perovskite onto the substrate, dissolving all precursors (MAI, PbI_2, CsBr, $PbBr_2$) in a mixed solvent (γ-butyrolactone: DMSO=7:3 vol%). After spin coating for a certain time, the film was treated with chlorobenzene. The doping content of Cs in the film, which was measured by ICP-AES (Table S1), could be linearly tuned through altering the composition of precursor solutions. As shown in the X-ray diffraction (XRD) spectra (Fig. 1a), for $(MAPbI_3)_{1-x}(CsPbBr_3)_x$, there was no additional $CsPbBr_3$ or $CsPbI_3$ orthorhombic phase observed in the film. For tetragonal phase of perovskite, due to the similar interplanar spacing, the peaks for (110) and (002) facets are highly close to each other, and so for (112) and (200) facets, thereby the two facets for corresponding peak were both labeled in the XRD spectra. Interestingly, the peaks for (112) and (200) facets substantially enhanced with the increasing doping content. For x=0 and 0.05, the major peaks are from (110)/(002) and (220)/(004) facets. In contrast, when x reached 0.1 and 0.2, the peaks for (112)/(200) and (224)/(400) facets dominated the whole pattern, indicating the film was oriented along <112> and <200> directions. In addition, the position of each peak, as shown in Table S2, shifted toward higher angle linearly as the doping content increased, indicating the decrease in lattice parameters. The lattice parameters of $MAPbI_3$ were calculated to be a=8.8706 Å and c=12.568 Å, consistent with the previous reports [22]. For x=0.1, the lattice parameters were a=8.8023 Å and c=12.4457 Å. The contraction of the unit cell was caused by the substitution MA^+ and I^- with smaller ionic radius of

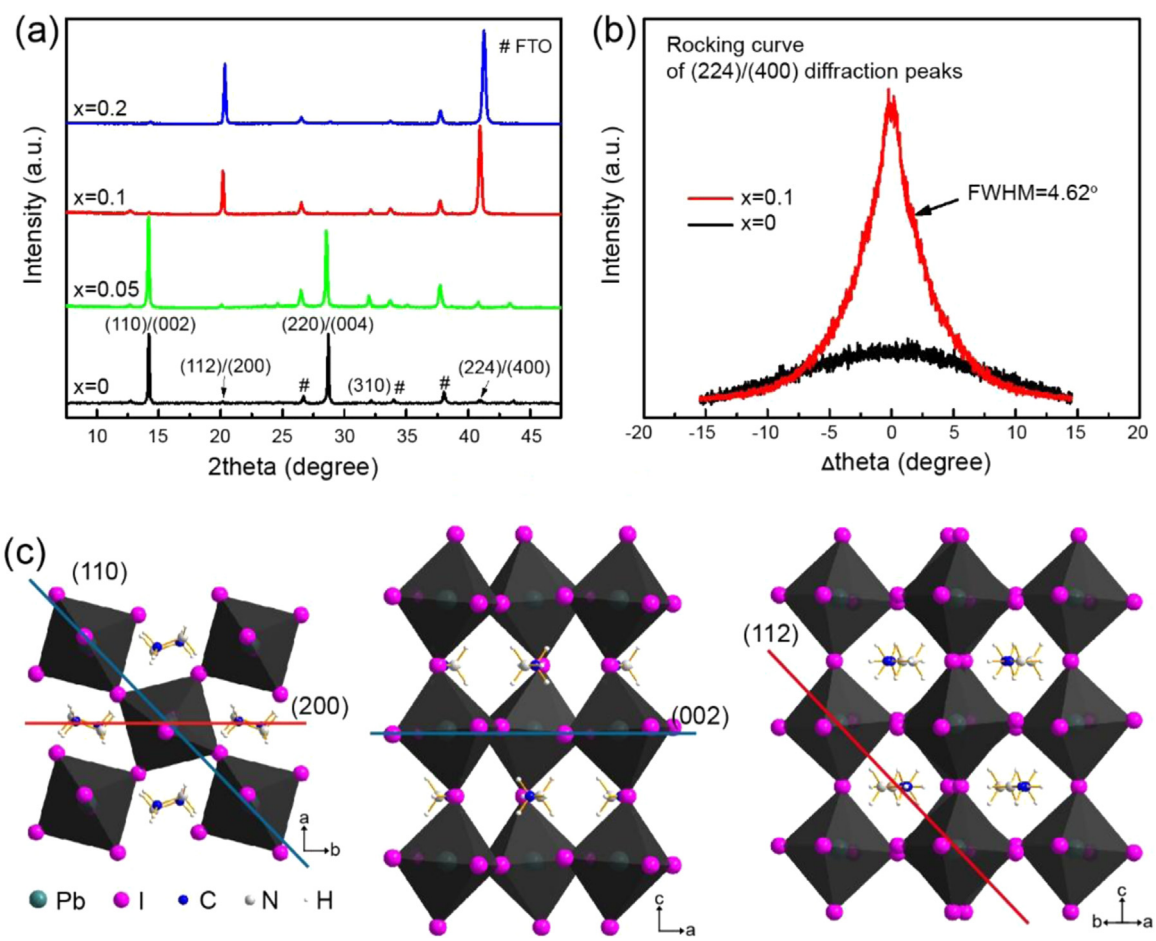

Fig. 1. (a) X-ray diffraction (XRD) patterns of fabricated perovskite films composed of $(MAPbI_3)_{1-x}(CsPbBr_3)_x$ with x ranging from 0 to 0.2. (b) Rocking curve measurement of (224)/(400) diffraction peaks for x=0 and 0.1. (c) Schematic illustrations of (110), (002), (112), and (200) crystal planes from a perpendicular view.

Cs^+ and Br^-, respectively. For x=0.2, the peaks for (112) and (200) facets merged together, implying the presence of cubic phase, instead of tetragonal phase, in the film. Therefore the position at 20.32° should be attributed to (110) facet as in cubic phase. Considering the similar atom arrangement and interplanar spacing between (112)/(200) facets in tetragonal phase and (110) facet in cubic phase, the peak was still labeled (112)/(200) to simplify the discussion. When the doping content increased to 0.3 and more, a new peak locating around 11.3° appeared, attributing to $CsPb_2Br_5$ phase (PDF# 25-0211), as shown in Fig. S1. The peaks for $CsPb_2Br_5$ gradually enhanced as x increased from 0.3 to 0.5.

The orientation of the film was further verified by rocking curve measurement, which was typically used to study the existence of preferential growth axis and its spread on the azimuthal angle [23–25]. The film is rocked while the detector is kept a fixed 2θ angle to record diffraction intensities from the preferentially oriented lattice planes. Fig. 1b shows the rocking curve of (224)/(400) diffraction peaks for x=0 and 0.1. The analysis exhibited for x=0.1, (224)/(400) planes were parallel to the substrate with an angular spread around the growth axis of ±4.6° (full width at half maximum, abbreviated as FWHM), while for x=0, the rocking curve exhibited no peaks. A similar phenomenon was also observed in the rocking curve of (112)/(200) diffraction peaks (Fig. S2b). The rocking curves for (110)/(002) diffraction peaks demonstrated that for x=0, it was the (110)/(002) facets parallel to the substrate (Fig. S2a), consistent with the XRD results.

As shown in the schematics (Fig. 1c), in the tetragonal phase, one Pb atom is coordinated with six I atoms, while one MA group is located in the center of a distorted cubooctahedral pocket with 12 I atoms at the vertices, enclosed by eight PbI_6 octahedra. As labeled in blue lines, both (110) and (002) planes involve two kinds of stacking layers that one is composed of Pb and I atoms, and the other is composed of MA groups and I atoms. In contrast, (112) and (200) planes involve only one kind of stacking layer, composed of Pb, I, and MA, as labeled in red lines. The surface energy of (110)/(002) and (112)/(200) planes is expected to be different due to the distinct coordination numbers of the surface atoms for each plane. A recent theoretical study discovered that for pure $MAPbI_3$, the crystal surface energy of (001) plane is lower than that of (100) plane, indicating (001) plane is more stable than (100) plane to achieve the lowest Gibbs free energy in view of the thermodynamic control [19]. When doping Cs into the crystal, the surface energy of each plane is expected to change since the electrostatic interaction of Cs–I is different from MA–I. The discussion about the surface energy will be illustrated later.

To gain more understanding of the origin of the oriented films along <112>/<200> directions, we used X-ray photoelectron spectra (XPS) depth profile analysis to obtain quantitative information. Fig. 2a shows the in-depth distribution of the atomic percentages as a function of the sputtering time for perovskite film with x=0.1. Before etching time reached 800 s, the atomic ratio of (I+Br)/Pb ranged from 2 to 3, whereas after 800 s, the ratio dropped below 2, which was also observed for $MAPbI_3$ film (Fig. S3), indicating the halide deficiency in the film. It is worth noting that there was a sudden rise of Cs/Pb atomic ratio for the perovskite film when sputtered for 800 s (Fig. 2b). Before 800 s,

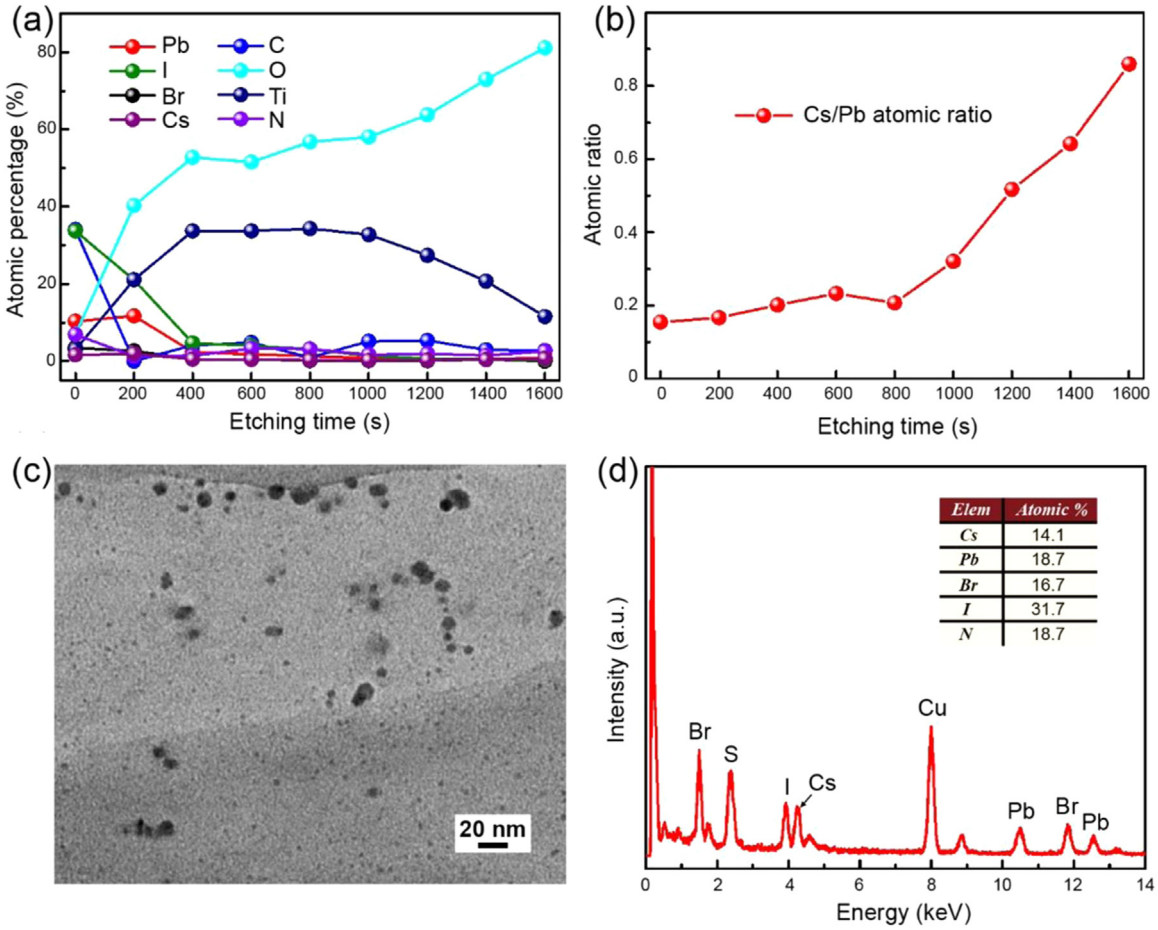

Fig. 2. (a) X-ray photoelectron spectra (XPS) depth profile analysis for perovskite film with x=0.1. (b) The calculated Cs/Pb atomic ratio of the film. (c) Transmission electron microscopy (TEM) image of the nanoparticles obtained by titrating chlorobenzene into the precursor solution. (d) Energy-dispersive spectroscopy (EDX) of the nanoparticles shown in (c). The inset shows the related atomic compositions.

the atomic ratio of Cs/Pb was around 0.15, slightly higher than that for the whole film. After 800 s, the atomic ratio of Cs/Pb gradually rose to 0.8–1.0 in the bottom of the film. The rise of Cs/Pb atomic ratio in the bottom was also verified by Auger electron spectroscopy (AES) depth profile analysis, with a Cs/Pb ratio around 0.8–1.2 in the bottom of the film (Fig. S4). The co-precipitation of Cs and Pb atoms in the bottom layer, and the XRD patterns, both verified the doping of Cs into perovskite, rather than forming a modification layer of CsBr or CsI as documented in previous reports [10]. In contrast, for x = 0, the atomic ratio of N/Pb, where the amount of N atoms was equal to MA, fluctuated around 1, which was consistent with the expected ratio in the stoichiometric crystal (Fig. S3b). It is proposed that CsX together with PbX_2 preferentially precipitated from the solution to form heavily Cs-doped perovskite onto the substrate during film formation process.

In order to further verify the assumption, we gradually titrated chlorobenzene into a solution containing CsBr, MAI, PbI_2, $PbBr_2$ in a mixed solvent (γ-butyrolactone: DMSO = 7: 3 vol%). Chlorobenzene, a well-known antisolvent for perovskite, is commonly used for inducing the fast precipitation of perovskite. After titrating a few drops of chlorobenzene, several sediments started to appear in the solution. Sequentially, the sediments, which represented the nucleation sites in the early stage of the crystallization process, were collected through centrifuging and vacuum drying for transmission electron microscopy (TEM) and energy-dispersive spectroscopy (EDX) study. It can be seen from Fig. 2c that the collected sediments were composed of nanoparticles with a wide size distribution, ranging from 6 to 20 nm. The EDX spectra (Fig. 2d) exhibited the composition of the particles, containing 14.1% Cs, 18.7% Pb, 31.7% I, 16.7% Br, and 18.7% N, with carbon and copper excluded. The calculated Cs/Pb ratio was 0.75, which is close to the ratio observed in the bottom layer of the film, proving the precipitation of $CsPbX_3$ or heavily Cs-doped perovskite in the early stage.

Based on the above observations, it was concluded that a heavily Cs-doped perovskite preferentially formed in the bottom layer of the film. Compared to MAX, CsX has a lower solubility in the solvent. Therefore during spin coating, as the solvent gradually evaporated, CsX together with PbX_2 preferentially precipitated. However, the origin of orientation along $<112>/<200>$ directions is still not clear, since both Cs and Br presented in the precursors. Therefore, we fabricated perovskite films from precursors containing only PbI_2, MAI, and CsI to exclude the effect of Br (Fig. S5a). The relative intensity of (112)/(200) to (110)/(002) was also increased, similar as that of $(MAPbI_3)_{1-x}(CsPbBr_3)_x$, manifesting the enhanced orientation along $<112>/<200>$ directions. In contrast, the perovskite film from precursors containing PbI_2, MAI, $PbBr_2$, excluding Cs atoms, displayed unchanged relative intensity of (112)/(200) to (110)/(002) (Fig. S5b). In addition, several independent researches also reported the different orientation directions when Cs was involved into the perovskite films [12,15]. Taken together, the orientation was believed to be caused by the presence of Cs salts in the precursor solutions and subsequent preferentially precipitated heavily Cs-doped perovskite at or near perovskite/TiO_2 interface.

According to a previous study, the film orientation direction is related to the crystal surface energy [19]. For tetragonal phase $MAPbI_3$, (001) plane is the most stable configurations, consistent with the film orientation directions. We calculated the crystal surface energy of (112), (100), (110), and (001) planes for tetragonal phase $CsPbBr_3$ using density functional theory. The details was shown in Supplementary information. It was interestingly found that (100) ($\gamma = 0.299\ J\ m^{-2}$) and (112) ($\gamma = 0.314\ J\ m^{-2}$) planes were more stable than (110) ($\gamma = 0.437\ J\ m^{-2}$) and (001) ($\gamma = 0.526\ J\ m^{-2}$) planes. Thereby, we believe in this work, the heavily Cs-doped perovskite could initiate the film growth along $<112>/<200>$ directions under thermodynamic control.

The optical properties were also studied for $(MAPbI_3)_{1-x}(CsPbBr_3)_x$ with x ranging from 0 to 0.5. As the doping content increased, the absorption onset shifted to a lower wavelength, caused by the incorporation of Br and Cs into the crystals (Fig. S7). Time-resolved photoluminescence (PL) spectra, recorded through a fluorescence microscopy, was utilized to monitor the change of the trap states in perovskite films, as shown in Fig. 3b. The curves were fitted with a biexponential decay function. The fast component is attributed to the surface recombination, while the slow component is caused by the recombination in the bulk of perovskite [26]. The lifetime of carriers was calculated by averaging the two components according to their amplitude. The average corresponding decay time was 2.04, 3.02, 4.01, and 4.89 ns for x = 0, 0.05, 0.1, and 0.2, respectively, as shown in the inset of Fig. 3b. The time scale obtained through fluorescence microscopy was consistent with the macroscopic time-resolved PL decays for $MAPbI_3$ [4,27]. The prolonged lifetime as x increased illustrated the reduction of trap density in the perovskite film, which was indicative of fewer non-radiative recombination sites [20,27]. According to previous reports, both Cs doping and orientation along $<112>/<200>$ directions are responsible for the reduction of trap states [12,20,21].

As shown in Fig. 3a, the cross-sectional SEM image of the device exhibited a clear planar structure, constructed with a 100 nm thick mesoporous TiO_2 (mp-TiO_2), a 360 nm thick perovskite layer, a 350 nm spiro-MeOTAD layer, and a 50 nm thick Au layer as the back contact. The perovskite films were ultra smooth, regardless of the increase of doping content (Fig. S9). As the Cs content increased, the films exhibited slightly larger crystal sizes. Nam-Gyu Park and co-workers observed similar phenomenon that $FA_{0.9}Cs_{0.1}PbI_3$ films showed larger crystals compared to $FAPbI_3$ films [12]. We propose a possible mechanism based on our results and previous studies by Michael Gratzel and Chun-Wei Chen [28,29]. For samples without Cs doping, the nucleation sites of perovskite were located on TiO_2 surface, while the following growth was restricted to limited space near the nucleation site, leading to small crystals. In contrast, when Cs was introduced into the precursors, Cs-induced precipitation, as verified by XPS depth scan and EDX analysis, functioned as effective nucleation sites. Then the heterogeneous growth started and the number of nucleation sites near TiO_2 surface could be suppressed, causing larger crystalline domains. The elemental distribution mapping of the perovskite film, as shown in Fig. S10, demonstrates the homogeneous distribution of Cs and Br atoms from the top-down view. The devices were measured under simulated AM 1.5 G illumination (100 mW cm^{-2}). The photovoltaic performance of perovskite solar cells with x = 0, 0.05, 0.1, and 0.2 was compared in Table 1. For x = 0, the devices have an average PCE of 14.5 ± 0.58%, with a J_{sc} of 22.6 ± 0.45 mA cm^{-2}, a V_{oc} of 1.00 ± 0.01 V, and a FF of 0.64 ± 0.03. As the doping content increased, J_{sc} gradually decreased. The external quantum efficiency (EQE) spectra showed the photoresponse range of each cell (Fig. 3c). As more Cs and Br incorporated into the crystals, the absorption band edge shifted to a shorter wavelength, directly causing the reduction of short circuit current. The integrated photocurrent density from EQE spectra was in accordance with the J_{sc} values for each cell. In contrast, both V_{oc} and FF gradually enhanced as x increased. Overall, the optimal doping content was x = 0.1, with an average PCE of 15.9%. Fig. 3e shows the J–V curve of the best cell, with a J_{sc} of 22.8 mA cm^{-2}, a V_{oc} of 1.05 V, and a FF of 0.73, resulting in a high performance of 17.6%. To rule out the influence of hysteresis effects on the transient photocurrent, the stabilized power output (SPO) is typically used by measuring the power output over time until reaching a steady value. The champion cell exhibited a SPO PCE of 15.7% and photocurrent of 19.6 mA cm^{-2}, when measured at 0.8 V (Fig. 3f).

In order to interpret the improvement of FF, series resistance (R_s) was derived from the J–V curves of the corresponding device,

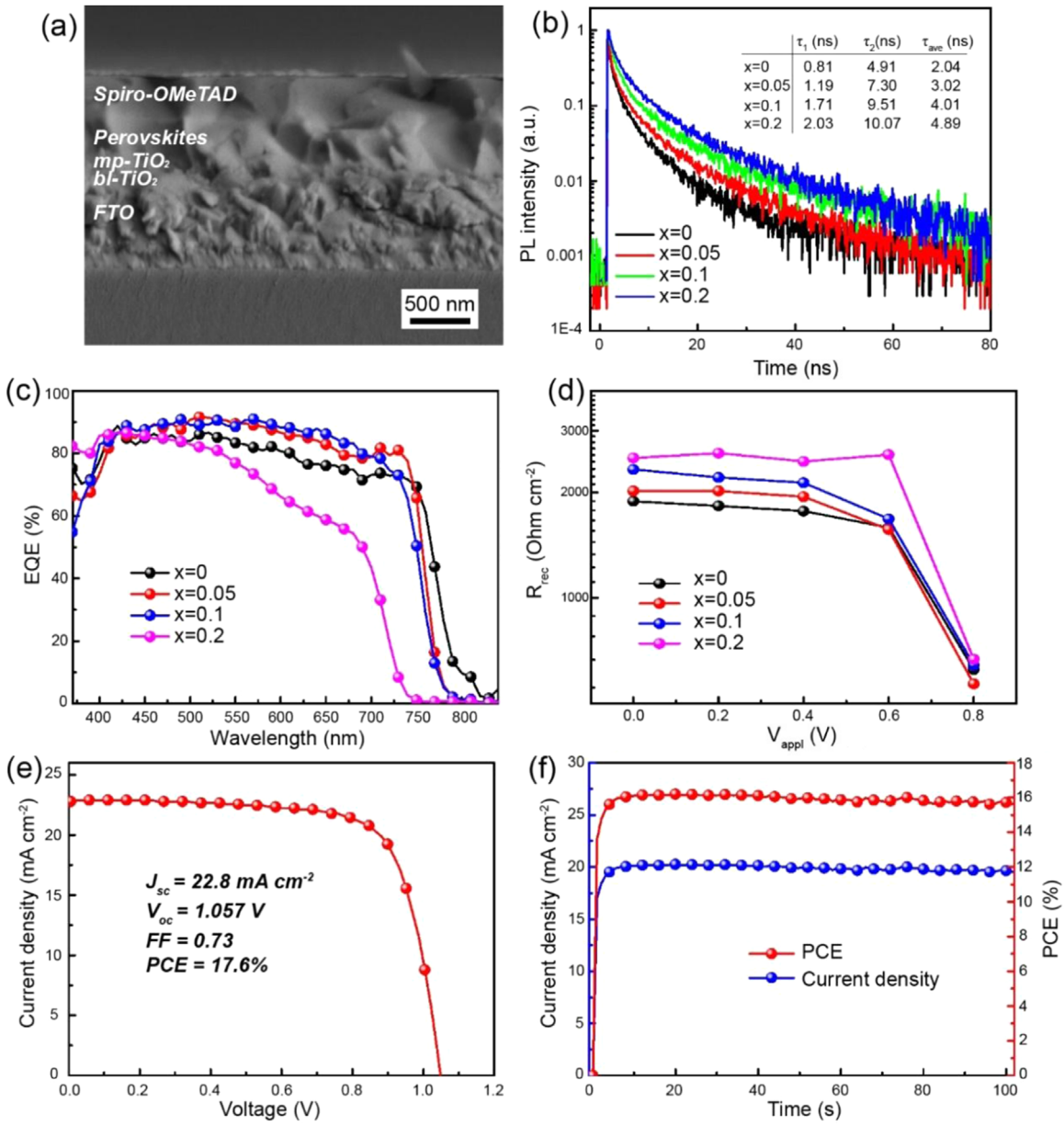

Fig. 3. (a) Cross-sectional SEM images of the fabricated solar cells. (b) Time-resolved photoluminescence (PL) spectra for the perovskite films with different doping content deposited on glass. The inset shows the lifetime fitted with a biexponential decay function. (c) External quantum efficiency (EQE) spectra for perovskite solar cells with different doping content. (d) Recombination resistance as a function of V_{appl} for each solar cell, derived from electrochemical impedance spectroscopy (EIS). (e) J–V curve of the best performing perovskite solar cell for x=0.1, collected at reverse scan with an aperture mask area of 0.09 cm^2. (f) Photocurrent density and power conversion efficiency as a function of time for the cell in (e) at 0.8 V forward bias.

Table 1
Photovoltaic performance for perovskite solar cells with different doping content, where each data was averaged from 8 devices.

	J_{sc} (mA cm^{-2})	V_{oc} (V)	FF	PCE (%)
x=0	22.6 ± 0.45	1.00 ± 0.01	0.64 ± 0.03	14.5 ± 0.58
x=0.05	22.3 ± 0.64	1.02 ± 0.02	0.66 ± 0.01	14.9 ± 0.80
x=0.1	20.9 ± 0.42	1.07 ± 0.01	0.71 ± 0.02	15.9 ± 0.52
x=0.2	17.2 ± 1.11	1.06 ± 0.03	0.70 ± 0.03	12.7 ± 1.61

as shown in Table S4. R_s typically represents the integral conductivity of the device correlated to the internal carrier mobility [30]. The oriented films along <112> and <200> directions exhibited series resistance of 12.2 Ω cm^{-2} and 16.2 Ω cm^{-2} for x=0.1 and 0.2, respectively. In contrast, the films oriented along <110> and <002> directions showed higher R_s values, 48.6 Ω cm^{-2} for x=0 and 0.05. This can be inferred that it is the orientation directions, rather than doping species (Cs and Br), play a predominant role in determining the internal charge transfer and series resistance, which is in line with the previous theoretical calculation results [19]. The enhancement of V_{oc} could be ascribed to two possible reasons, the increased band gap and suppressed charge recombination process. UV–Vis absorption spectra suggested the widening of the band gap with increasing x. The electrochemical impedance spectra (EIS) was performed to investigate the charge recombination process of the devices. The response under light conditions was analyzed at different applied voltages. Two semicircles and a low frequency feature are observed in the spectra at a certain applied voltage (Fig. S11). The first arc at higher frequencies attributes to the charge transfer in hole transport materials (HTM). The second one at lower frequencies is caused by

the electron recombination at the interface of TiO_2/perovskite/HTM. The low frequency feature is due to slow charge transport, which is not related to the device physics, and is not included in the analysis in this paper [31]. The impedance spectra was fitted with a simplified equivalent circuit from the typical transmission line model for dye sensitized solar cells, as shown in the inset of Fig. S11a. The R_{rec} from the second arc represents the charge recombination barrier at the interface of TiO_2/perovskite/HTM. It is well acknowledged that a higher R_{rec} leads to a higher V_{oc} [32]. In this work, R_{rec} exhibited an obvious uplift with increasing x in the whole V_{appl} range (Fig. 3d), indicating severer suppression of charge recombination at the interface, which explained the enhancement of V_{oc}. The reduced charge recombination was owing to the decreased trap states in the perovskite film, which has been proved by PL spectra. Moreover, it could be seen that as the V_{appl} increased, the recombination resistance lowered, because of the upshift of the Fermi level of TiO_2 and promoted electron transfer to perovskite and HTM.

The stability of perovskite solar cells is a current major issue restricting the terrestrial applications. The accelerated stability of the devices is evaluated under UV irradiation without encapsulation (Fig. 4a). The cells were exposed to 365 nm UV illumination (364 mW cm^{-2}) for a certain time, and then measured with a standard J–V characterization method. It could be concluded that as x increased, the stability was significantly improved. For $(MAPbI_3)_{0.9}(CsPbBr_3)_{0.1}$, 75% of the initial performance was maintained after 150 min irradiation. Conversely, the performance of $MAPbI_3$ declined to 11% of the original value in the same condition. According to the UV–Vis absorption spectra and XRD spectra (Figs. S12 and S13), the perovskite film after UV light degraded into PbI_2. The doping of $CsPbBr_3$ into the film could significantly reduce the degradation process. The degradation under UV light was reported to be caused by the TiO_2-mediated decomposition of perovskite, which was correlated with the non-radiative defect sites within the perovskite and especially at the TiO_2/perovskite interface [10]. As confirmed by PL and EIS results, the reduced trap density and thus suppressed TiO_2-mediated decomposition of perovskite, which was caused by the involvement of Cs and orientation along $<112>/<200>$ directions, was beneficial for the durability of perovskite solar cells under UV light conditions. Moreover, the heavily Cs-doped perovskite in the bottom of the film could also protect perovskite from degradation by UV irradiation [10]. In addition to the UV stability, we also measured the stability of the unencapsulated devices in an ambient environment at 25 °C and with 20–30% humidity (Fig. 4b). For pure $MAPbI_3$, the efficiency gradually decreased to ~30% of the initial value after exposing for 500 h. The degradation was mainly caused by the moisture ingress into the films and thereby accelerated MAI dissolution [8]. For $(MAPbI_3)_{0.9}(CsPbBr_3)_{0.1}$, the device exhibited greatly enhanced stability, with nearly 80% of the initial performance maintained after 500 h durability test. The improved durability was mainly ascribing to the incorporation of Cs and Br into the unit cell and contraction of the cell parameters. The contracted crystal structures are resistant to the invasion of moisture from the atmosphere [11].

3. Conclusions

To conclude, we have successfully fabricated oriented film of $(MAPbI_3)_{1-x}(CsPbBr_3)_x$ along $<112>/<200>$ directions. The altered orientation was found to be highly related to the crystallization process during film formation. Perovskite with higher content of Cs atoms precipitated preferentially, due to the limited solubility of CsX and PbX_2 in the solvent compared to MAX. According to the density functional calculations, the surface free energy of (100) and (112) planes are lower than (110) and (001) planes for tetragonal phase $CsPbBr_3$. Therefore, the preferentially precipitated heavily Cs-doped perovskite could initiate the growth along $<112>/<200>$ directions. The fabricated solar cells exhibited an optimal performance at x=0.1, with J_{sc} decreasing, while V_{oc} and FF increasing as the doping content increased. The reduced J_{sc} came from the limited absorption region after doping. The enhancement of FF was due to the improved charge transfer in the oriented film along $<112>/<200>$ directions and thus reduced series resistance. The suppressed trap states of perovskite, due to the orientation along $<112>/<200>$ directions as well as Cs involvement, helped restrain the internal charge recombination process and enhanced V_{oc}. In addition, the stability of $(MAPbI_3)_{0.9}(CsPbBr_3)_{0.1}$ toward UV light and moisture were substantially improved compared to $MAPbI_3$. The enhanced stability toward UV light resulted from the reduced trap states in perovskite, while the improved durability in moisture was attributed to the contraction of the unit cell as the incorporation of Cs and Br. The solar cells constructed from $(MAPbI_3)_{1-x}(CsPbBr_3)_x$ with high performance and stability are of great potential for practical applications. It is believed that the well-controlled orientation through mixed cations provides a versatile tool to further improve

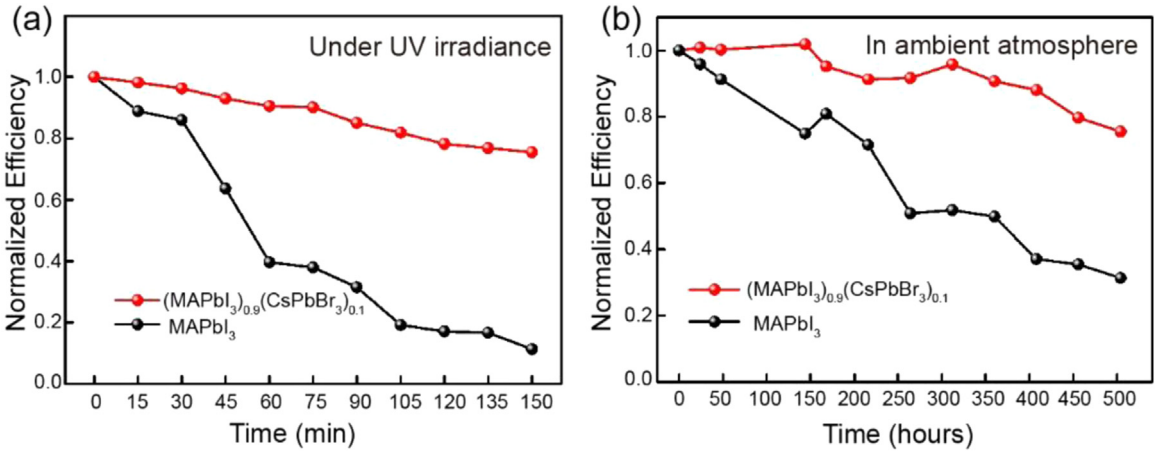

Fig. 4. Stability test for $MAPbI_3$ and $(MAPbI_3)_{0.9}(CsPbBr_3)_{0.1}$ (a) under 365 nm UV illumination (364 mW cm^{-2}) and (b) in an ambient atmosphere (dark, 25 °C, 20–30% humidity) without encapsulation.

the photovoltaic performance. Further study on fabricating $FAPbI_3$ perovskite films with well-controlled orientations to compensate the loss of photocurrent is still underway.

4. Experimental section

4.1. Solar cell fabrications

The TiO_2 compact layer was deposited onto FTO glass through atomic layer deposition (Beneq TFS 200) documented in previous reports. The mp-TiO_2 layer was prepared by depositing nanocrystalline TiO_2 paste (18NRT from Dyesol Company; diluted to w/w 14.3%) onto the compact layer at 6000 rpm for 30 s followed by heating at 500 °C for 1 h. The perovskite precursors were prepared by dissolving PbI_2, MAI, $PbBr_2$, and CsBr in the mixed solvent (γ-butyrolactone: DMSO=7: 3 vol%). For x=0, the concentration was 0.96 M for both PbI_2 and MAI. For x=0.05, the concentration of PbI_2 and MAI was 0.912 M, and that of $PbBr_2$ and CsBr was 0.048 M. For x=0.1, the concentration of PbI_2 and MAI was 0.753 M, and that of $PbBr_2$ and CsBr was 0.089 M. For x=0.2, the concentration of PbI_2 and MAI was 0.672 M, and that of $PbBr_2$ and CsBr was 0.168 M. The solutions were then coated onto the substrate by two consecutive spin-coating steps, at 1500 rpm for 10 s, and 5000 rpm for 30 s. During the second step, 0.3 mL chlorobenzene was poured onto the substrate. Then the film was heated at 70 °C for 30 min, 110 °C for 30 min, and 150 °C for 10 min. Spiro-MeOTAD solution was prepared by dissolving 102.7 mg spiro-MeOTAD in 1 mL chlorobenzene, to which 9.85 μL 4-tert-butyl pyridine and 42.22 μL lithium bis(trifluoromethanesulfonyl)imide solution (170 mg LITFSI in 1 mL acetonitrile) were added. Spiro-MeOTAD was deposited on the substrate at 2000 rpm for 45 s. Then the films were left in air overnight. Finally, 50 nm gold electrode were thermally evaporated under vacuum of $\sim 10^{-6}$ Torr, at a rate of ~0.2 Å/s.

4.2. Characterization

X-ray diffraction (XRD) spectra was measured with smart LAB instruments Cu Kα beam (λ=1.54 Å). UV–Vis absorption spectra were obtained with a Hitachi U-3010 spectroscope. SEM images were measured by JEOL JSM-7401 F and TEM images by Hitachi HT7700 with an acceleration voltage of 100 kV. The composition of the film was measured by ICP-AES (Thermo IRIS intrepid II). XPS depth profiling was measured by ESCALAB 250Xi, Thermo Scientific, sputtered by Ar^+. AES depth profiling was measured by PHI-700, ULVAC-PHI, sputtered by Ar^+. J–V curves were measured by a Keithley 2400 source meter under one sun illumination (AM 1.5 G, 100 mW cm^{-2}), simulated by a solar simulator (ORIEL 81193) calibrated with an NREL-calibrated silicon solar cell. External quantum efficiency (EQE) spectra were recorded by a setup, consist of a xenon light source, a monochromator, and a potentiostat. EIS were measured by an electrochemical workstation (Zahner, CIMPS) with frequency from 10 to 10^6 Hz under applied voltage with an amplitude of 10 mV under light condition. The active area of each cell was 0.16 cm^2 with a mask of 0.09 cm^2. Time-resolved PL decay was measured by a FV1200, excited at 488 nm.

Acknowledgments

The research was funded by the National Natural Science Foundation of China under Grant nos. 51273104 and 91433205.

Appendix A. Supporting information

Supplementary data associated with this article can be found in the online version at http://dx.doi.org/10.1016/j.nanoen.2016.06.053.

References

[1] H.S. Kim, C.R. Lee, J.H. Im, K.B. Lee, T. Moehl, A. Marchioro, S.J. Moon, R. Humphry-Baker, J.H. Yum, J.E. Moser, M. Gratzel, N.G. Park, Sci. Rep. 2 (2012) 591.
[2] W.S. Yang, J.H. Noh, N.J. Jeon, Y.C. Kim, S. Ryu, J. Seo, S.I. Seok, Science 348 (2015) 1234–1237.
[3] ⟨http://www.nrel.gov/ncpv/images/efficiency_chart.jpg⟩.
[4] G. Xing, N. Mathews, S. Sun, S.S. Lim, Y.M. Lam, M. Gratzel, S. Mhaisalkar, T. C. Sum, Science 342 (2013) 344–347.
[5] M. Gratzel, Nat. Mater. 13 (2014) 838–842.
[6] N.J. Jeon, J.H. Noh, W.S. Yang, Y.C. Kim, S. Ryu, J. Seo, S.I. Seok, Nature 517 (2015) 476–480.
[7] G. Niu, X. Guo, L. Wang, J. Mater. Chem. A 3 (2015) 8970–8980.
[8] G. Niu, W. Li, F. Meng, L. Wang, H. Dong, Y. Qiu, J. Mater. Chem. A 2 (2014) 705–710.
[9] G.E. Eperon, S.D. Stranks, C. Menelaou, M.B. Johnston, L.M. Herz, H.J. Snaith, Energy Environ. Sci. 7 (2014) 982–988.
[10] W. Li, W. Zhang, S. Van Reenen, R.J. Sutton, J. Fan, A.A. Haghighirad, M. B. Johnston, L. Wang, H.J. Snaith, Energy Environ. Sci. 9 (2016) 490–498.
[11] J.H. Noh, S.H. Im, J.H. Heo, T.N. Mandal, S.I. Seok, Nano Lett. 13 (2013) 1764–1769.
[12] J.W. Lee, D.H. Kim, H.S. Kim, S.W. Seo, S.M. Cho, N.G. Park, Adv. Energy Mater. 5 (2015) 1501310.
[13] H. Choi, J. Jeong, H.-B. Kim, S. Kim, B. Walker, G.-H. Kim, J.Y. Kim, Nano Energy 7 (2014) 80–85.
[14] E.L. Unger, A.R. Bowring, C.J. Tassone, V.L. Pool, A. Gold-Parker, R. Cheacharoen, K. H. Stone, E.T. Hoke, M.F. Toney, M.D. McGehee, Chem. Mater. 26 (2014) 7158–7165.
[15] G.E. Eperon, G.M. Paternò, R.J. Sutton, A. Zampetti, A.A. Haghighirad, F. Cacialli, H.J. Snaith, J. Mater. Chem. A 3 (2015) 19688–19695.
[16] C. Yi, J. Luo, S. Meloni, A. Boziki, N. Ashari-Astani, C. Gratzel, S.M. Zakeeruddin, U. Röthlisberger, M. Gratzel, Energy Environ. Sci. 9 (2016) 656–662.
[17] J.A. Koza, J.C. Hill, A.C. Demster, J.A. Switzer, Chem. Mater. 28 (2016) 399–405.
[18] E. Mosconi, E. Ronca, F. De Angelis, J. Phys. Chem. Lett. 5 (2014) 2619–2625.
[19] J. Yin, D. Cortecchia, A. Krishna, S. Chen, N. Mathews, A.C. Grimsdale, C. Soci, J. Phys. Chem. Lett. 6 (2015) 1396–1402.
[20] Q. Liang, J. Liu, Z. Cheng, Y. Li, L. Chen, R. Zhang, J. Zhang, Y. Han, J. Mater. Chem. A 4 (2016) 223–232.
[21] S. Bae, S.J. Han, T.J. Shin, W.H. Jo, J. Mater. Chem. A 3 (2015) 23964–23972.
[22] T. Baikie, Y. Fang, J.M. Kadro, M. Schreyer, F. Wei, S.G. Mhaisalkar, M. Gratzel, T. J. White, J. Mater. Chem. A 1 (2013) 5628–5641.
[23] G. Pellegrino, S. Colella, I. Deretzis, G.G. Condorelli, E. Smecca, G. Gigli, A. La Magna, A. Alberti, J. Phys. Chem. C 119 (2015) 19808–19816.
[24] A. Ishii, A.K. Jena, T. Miyasaka, A.P.L. Mater, 2 (2014) 091102.
[25] M. Yasaka, J. Rigaku, vol. 26, 2010, p. 2.
[26] M.I. Saidaminov, A.L. Abdelhady, B. Murali, E. Alarousu, V.M. Burlakov, W. Peng, I. Dursun, L. Wang, Y. He, G. Maculan, A. Goriely, T. Wu, O. F. Mohammed, O.M. Bakr, Nat. Commun. 6 (2015) 7586.
[27] S.D. Stranks, G.E. Eperon, G. Grancini, C. Menelaou, M.J. Alcocer, T. Leijtens, L. M. Herz, A. Petrozza, H.J. Snaith, Science 342 (2013) 341–344.
[28] M. Saliba, T. Matsui, J.-Y. Seo, K. Domanski, J.-P. Correa-Baena, M. K. Nazeeruddin, S.M. Zakeeruddin, W. Tress, A. Abate, A. Hagfeldt, M. Gratzel, Energy Environ. Sci. 9 (2016) 1989–1997.
[29] S.-S. Li, C.-H. Chang, Y.-C. Wang, C.-W. Lin, P.-Y. Wang, J.-C. Lin, C.-C. Chen, H.-S. Sheu, H.-C. Chia, W.-R. Wu, U.-S. Jeng, C.-T. Liang, R. Sankar, F.-C. Chou, C.-W. Chen, Energy Environ. Sci. 9 (2016) 1282–1289.
[30] C.-G. Wu, C.-H. Chiang, Z.-L. Tseng, M.K. Nazeeruddin, A. Hagfeldt, M. Gratzel, Energy Environ. Sci. 8 (2015) 2725–2733.
[31] H.-S. Kim, J.-W. Lee, N. Yantara, P.P. Boix, S.A. Kulkarni, S. Mhaisalkar, M. Gratzel, N.-G. Park, Nano Lett. 13 (2013) 2412–2417.
[32] B. Suarez, V. Gonzalez-Pedro, T.S. Ripolles, R.S. Sanchez, L. Otero, I. Mora-Sero, J. Phys. Chem. Lett. 5 (2014) 1628–1635.

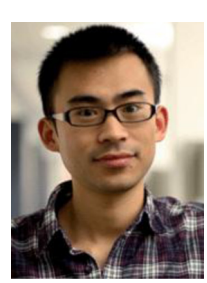

Guangda Niu was born in Hebei, China, in 1988. He received a BS degree in Chemistry (2011) from Nanjing University. Since then, he has been pursuing his Ph.D degree at Tsinghua University under the supervision of Prof. Liduo Wang. His research interests include the rational design of inorganic–organic hybrid perovskite solar cells, quantum dot sensitized solar cells, and controlled synthesis of nanomaterials.

Hongde Yu graduated with a BS degree majoring in chemistry from Tsinghua University, Beijing, China in 2015 and is presently a graduate student under the supervision of Prof. Dong Wang at Tsinghua University. His research interests are computer simulations of self-assembly in soft matter.

Dong Wang received her Ph.D in physical chemistry from the University of Science and Technology of China in 2000. She then worked as postdoc with Prof. Eitan Geva at the University of Michigan and with Prof. Greg Voth at the University of Utah. She became an associate professor at Tsinghua University in 2010. Her research interests include theoretical investigation of thermoelectric transport in organic materials and computer simulations of self-assembly phenomena.

Jiangwei Li graduated with a BS degree majoring in chemistry from Tsinghua University, Beijing, China in 2014 and is currently a graduate student in Prof. Liduo Wang's group at Tsinghua University. His research interests include rational design and stability study of perovskite solar cells.

Liduo Wang is a professor of the Department of Chemistry in Tsinghua University. He received his Ph.D degree in Nagoya University of Japan in 1995. Dr Wang has once worked as a visiting scholar in the Department of Chemistry and as the research associate in the Department of Electrical and Electronic Engineering in The Hong Kong University of Science and Technology, and as a postdoctoral researcher in Department of Materials Science and Engineering, Tsinghua University. His current research interests include perovskite solar cells, organic–inorganic semiconductor multilayer, and its optoelectronic properties.